INORGANIC CHEMISTRY FRONTIERS

RESEARCH ARTICLE

View Article Online
View Journal

Cite this: DOI: 10.1039/d5qi01971k

Real-time vibrational fingerprinting of liquid-phase sulfide electrolyte synthesis *via in situ* Raman spectroscopy

Zachary Warren, [a,b] Thomas Poupeau, [c] Beyza Batu [d] and Nataly Carolina Rosero-Navarro *[a]

All-solid-state lithium batteries benefit from scalable routes to sulfide solid electrolytes with controlled phase formation. Here, an *in situ* Raman spectrometer integrated with a microwave reactor provides real-time vibrational fingerprints of the liquid-phase reaction between Li_2S and P_4S_{10} in acetonitrile. We benchmark the cell by tracking P_4S_{10} solubility up to 130 °C and establish analytical performance for the P═S stretch at ~716 cm^{-1}, determining LOD = 0.78 mM and LOQ = 2.60 mM. Time-resolved spectra capture the systematic decay of the 716 cm^{-1} band during the reaction, consistent with the disruption of the P_4S_{10} cage and formation of thiophosphate intermediates. Early-stage kinetics are quantitatively described by the Finke–Watzky two-step model, and temperature-dependent rate constants yield Arrhenius and Eyring relationships with E_a(mw) = 39.59 kJ mol^{-1}, $\Delta H^{\ddagger}$ = 36.97 kJ mol^{-1}, and $\Delta S^{\ddagger}$ = −178.55 J mol^{-1} K^{-1}. This combined *in situ* spectroscopic–kinetic approach offers a direct pathway to mechanistic understanding and parameter extraction in solution-based synthesis of sulfide SSEs.

Received 25th September 2025,
Accepted 23rd November 2025

DOI: 10.1039/d5qi01971k

rsc.li/frontiers-inorganic

Introduction

The global demand for safer, more energy-dense, and longer-lasting energy storage systems has propelled all-solid-state lithium-ion batteries (ASSLiBs) to the forefront of research and development. Unlike conventional lithium-ion batteries (LIBs), which rely on liquid electrolytes, ASSLiBs utilize solid-state electrolytes (SSEs) to transport lithium ions, offering transformative improvements in safety and performance. Notably, the complete absence of flammable liquid electrolytes in ASSLiBs renders them inherently non-flammable, mitigating the risk of thermal runaway and catastrophic failure—a persistent issue in traditional LIBs. Beyond safety, the use of solid-state electrolytes enables the adoption of lithium metal anodes, significantly improving energy density due to the high capacity of lithium metal compared to those of conventional anode materials.[1] These advancements collectively position ASSLiBs as a key technology for next-generation energy storage, underpinning critical applications in electric vehicles, grid storage, and portable electronics.

Among the various materials explored for SSEs, sulfide-based solid electrolytes (SSEs) have garnered particular attention due to their remarkable ionic conductivities, which can reach conductivities similar to liquid electrolytes.[2] Sulfide SSEs, such as those derived from lithium thiophosphates (*e.g.*, LPS systems), exhibit additional advantages, including low grain boundary resistance, excellent processability, and compatibility with high-voltage cathodes.[3] These properties make sulfide SSEs especially appealing for integration into ASSLiBs, where both ionic conductivity and electrochemical stability are critical to device performance. However, despite these promising attributes, significant challenges remain in the synthesis and large-scale production of sulfide SSEs.

Conventional synthetic methods for sulfide SSEs, such as mechanical ball-milling and melt-quenching, are energy-intensive and time-consuming, due to their dependence on prolonged processing times and high-temperature conditions. These drawbacks present bottlenecks for commercialization and have spurred the search for alternative synthesis strategies that are scalable, efficient, and capable of producing high-performance materials. In recent years, solution-based suspension synthesis has emerged as a compelling alternative, offering rapid, low-temperature processing of sulfide SSEs. This method employs polar organic solvents to mediate the reaction between precursor materials, significantly reducing

[a]*Instituto de Cerámica y Vidrio–CSIC, C/Kelsen 5, Madrid, 28049, Spain. E-mail: rosero@icv.csic.es*
[b]*Universidad Autónoma de Madrid, Ciudad Universitaria de Cantoblanco, 28049 Madrid, Spain*
[c]*Département Matériaux – Campus de Luminy 163 avenue de Luminy, case 925, 13288 Marseille Cedex 09, France*
[d]*Sakarya University, Department of Metallurgical & Materials Engineering, Esentepe Campus, 54050 Sakarya, Turkey*

the energy requirements and processing times associated with traditional methods. Among the solvents explored, acetonitrile (ACN) has demonstrated notable success in facilitating the synthesis of LPS and LPSX (X = Cl, Br, I) systems, yielding materials with ionic conductivities up to 10^{-3} S cm^{-1}.[4,5]

While solution-based suspension synthesis represents a promising pathway for the scalable production of sulfide solid-state electrolytes (SSEs), the underlying mechanisms that govern these reactions remain poorly understood. Specifically, the role of the solvent in mediating the dissolution, nucleation, and growth of thiophosphate phases is not fully elucidated. Fundamental questions regarding the thermodynamics and kinetics of these processes, as well as the nature of intermediate species formed during synthesis, remain unanswered. Addressing these knowledge gaps is critical not only for optimizing synthetic protocols but also for ensuring the reproducibility and scalability of sulfide SSE production. Furthermore, a deeper understanding of these mechanisms could enable the rational design of new solvents and processing conditions tailored to specific electrolyte compositions and performance requirements.

Despite several mechanistic models having been proposed to describe the formation of thiophosphate networks in liquid media,[6–8] these frameworks often rely on indirect or *ex situ* evidence, leading to ambiguities in their interpretation. Many reported mechanisms assume a simple stepwise conversion from molecular precursors such as P_4S_{10} and Li_2S into terminal $[PS_4]^{3-}$ or bridging $[P_2S_7]^{4-}$ units, yet they fail to capture the complexity of intermediate speciation observed experimentally.

Furthermore, the proposed mechanisms rarely account for the dynamic equilibria between solubilized fragments, colloidal clusters, and precipitated products that can coexist during synthesis. The influence of solvent polarity, donor number, and Lewis basicity on the stabilization of these species remains largely speculative, as does the impact of reaction conditions such as temperature, stirring rate, and concentration gradients. Without direct *in situ* or *operando* evidence, these mechanistic descriptions remain qualitative and system-dependent, limiting their predictive power across different solvent systems or precursor ratios.

A comprehensive mechanistic understanding will therefore require integrating experimental and computational approaches capable of resolving short-lived intermediates, mapping reaction energy landscapes, and correlating the molecular structure with macroscopic properties. Such insight would not only clarify the limitations of current models but also pave the way for a truly rational, chemistry-driven design of next-generation sulfide electrolytes.

Advanced characterization techniques are indispensable for probing the complex chemical and physical processes that occur during the synthesis of sulfide SSEs. Among these techniques, *in situ* Raman spectroscopy stands out as a powerful method for real-time monitoring of chemical transformations. Raman spectroscopy, which is based on the inelastic scattering of photons, provides molecular-level insights into the vibrational modes of chemical species. This technique is particularly well-suited for studying sulfide-based materials due to its sensitivity to thiophosphate functional groups, which are the primary constituents of sulfide SSEs. By enabling the identification of reaction intermediates, phase transitions, and molecular interactions, *in situ* Raman spectroscopy offers a unique window into the dynamics of sulfide SSE synthesis.

The application of *in situ* Raman spectroscopy to the study of sulfide SSEs is not without precedent. Previous studies have demonstrated the utility of Raman spectroscopy for characterizing thiophosphate-based materials, revealing critical information about their structural and compositional properties.[9] For example, Raman analysis has been used to identify key vibrational modes associated with PS_4^{3-}, $P_2S_7^{2-}$, $P_2S_6^{2-}$ and $P_2S_6^{4-}$ anions,[10–13] which are characteristic of lithium thiophosphates. However, the potential of *in situ* Raman spectroscopy for unravelling the complex mechanisms of solution-based suspension synthesis remains largely untapped.

In this study, we utilized *in situ* Raman spectroscopy to investigate the synthesis of sulfide solid-state electrolytes (SSEs) through solution-based suspension processes. By monitoring the real-time reaction between Li_2S and P_2S_5 in acetonitrile, we aim to elucidate the underlying reaction kinetics and identify transient intermediates. This approach provides direct spectroscopic evidence of the chemical pathways involved in SSE formation. In parallel, we performed complementary kinetic analyses to develop a comprehensive understanding of the mechanisms and factors governing sulfide SSE synthesis.

Experimental

All chemical precursors, solvents, and reaction vessels were prepared in an argon-filled glovebox (O_2 < 0.5 ppm, H_2O < 0.5 ppm). Acetonitrile (ACN, Aldrich, 99.9%) was dried for 1 week using prewashed, heat-treated molecular sieves (Supelco, 3 μm). Lithium sulfide (Li_2S, Aldrich, 99.98%) and phosphorus pentasulfide (P_2S_5, Aldrich, 99.99%) were combined in three molar ratios (1 : 2, 2 : 2, and 3 : 2) to produce three pre-sulfide solid electrolyte (pSSE) mixtures.

The solubility of P_2S_5 in ACN was analyzed by heating the mixture from 30 to 130 °C in 10 °C increments, holding each step for 10 minutes using an Anton Paar Monowave 400 microwave reactor with mechanical stirring. *In situ* Raman spectra were collected with a Cora 5001 spectrometer (785 nm, fiber probe) integrated with the microwave reactor. Spectra were recorded at the end of each step to monitor changes.

Reactions of pSSEs in ACN were carried out at constant temperatures (35–50 °C) with stirring at 600 rpm for up to 1000 seconds. Reaction vials, containing pSSE, a magnetic stir bar, ACN, and PTFE-lined silicon septa, were prepared in the glovebox and sealed before use in the microwave reactor. Raman spectra were collected every 10 seconds (average of 6 scans) using a 785 nm laser at 450 mW with 1000 ms exposure.

Baseline correction and normalization of Raman spectra were performed using Cora 5001 software. Peak integration and analysis were carried out using the SciPy Python library.

Results and discussion

Solubility of P_4S_{10} and spectral monitoring

Microwave assisted reactions have been increasingly explored offering several advantages over conventional heating like rapid and instantaneous heating, high temperature homogeneity and selective heating.[14] Microwave heating works especially well with polar solvents like acetonitrile, tetrahydrofuran, and dimethoxymethane, which have all been reported for the synthesis of LPS SSEs without microwave irradiation.[15] Microwave reactor systems not only help control the temperature of synthetic processes in solvents, but also maintain constant power or pressure. When coupled with *in situ* Raman spectroscopy, it becomes a powerful tool in understanding the evolution of functional groups during reaction processes.

To validate the performance of the reaction cell and the *in situ* Raman spectroscopic setup, a solubility analysis of P_2S_5 in acetonitrile (ACN) was conducted. This test serves as a functional benchmark, confirming that the system can effectively monitor solid–liquid interactions in real time. Fig. 1 presents the Raman spectra collected during the dissolution process, demonstrating the spectrometer's sensitivity and the reactor's ability to maintain stable and reproducible mixing and sampling conditions.

Evidently, there is a lack of any significant change in the Raman signals present during the solubility analysis between 30 and 130 °C. It is worth mentioning that these temperatures far exceed the typically reported temperatures for liquid-phase synthesis of LPS, generally reported at room temperature or up to 50 °C. However, these higher temperatures are justifiable in studying the effects of the solubility of P_2S_5 in ACN. At these higher temperatures there is the inclusion of a shouldered signal at 392 cm^{-1}, which becomes noticeable at 90 °C, which is assigned to the P–S–P bend in the P_4S_{10} structure.[16] Above the boiling point of ACN (82 °C), acetonitrile undergoes significant volatilization, resulting in a reduced liquid-phase contribution to the Raman spectrum and thereby enhancing the relative intensity of the solid-phase P_4S_{10} vibrational mode observed at 392 cm^{-1}. The transition from the liquid to gas phase of the ACN in the reaction vessel is observed with the significant increase in reaction gas pressure illustrated in Fig. S1.

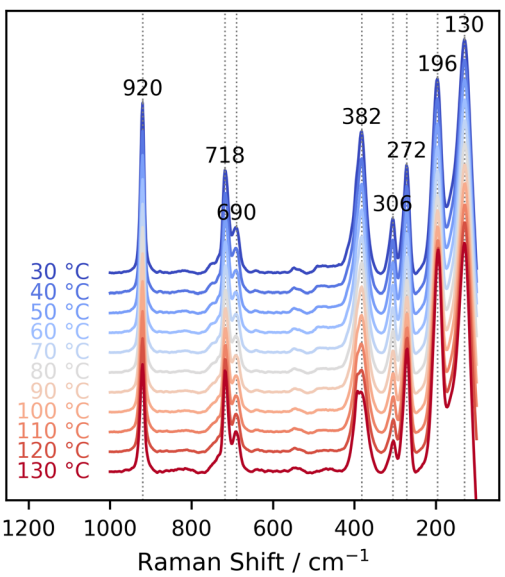

Fig. 1 The Raman spectra for P_2S_5 in acetonitrile and heated to temperatures between 30 and 130 °C by microwave irradiation at constant volume.

To better understand the spectra in Fig. 1, an explanation of signals for the reaction system is necessary. One caveat to the Cora 5001 with a 785 nm laser is that the signal measurements start at 100 cm^{-1} with an intensity of 0 AU. Because of this, during baseline correction and normalization, the spectra offer little quantitative data up to 250 cm^{-1} due to spectral deformation. The system analyzed in Fig. 1 exhibits peaks at 196 (broad), 272, 306, 382–392 (broad), 690, 718, and 920 cm^{-1}. Following tabulated data from comprehensive study with Raman spectroscopy for ACN, the peaks at 382 (ν_8; C–C≡N bend) and 920 cm^{-1} (ν_4; C–C stretch) have been assigned to acetonitrile.[17] However to discuss the remaining signals, it is important to illustrate P_2S_5 in its native state, P_4S_{10}. P_2S_5 is the ionic monomer of P_4S_{10}, and both are illustrated in Fig. 2.

Comprehensive theoretical experiments using Hartree–Fock, Møller–Plesset and density functional theory calculations examined the vibrational frequencies of the P_4S_{10} structure for IR and Raman spectroscopy, identifying possible signals exhibited by the P_4S_{10} structure.[16] Therefore, the remaining Raman signals illustrated in Fig. 1 were assigned to the vibrational nodes of P_4S_{10}: 130 cm^{-1} (P═S wag), 196 cm^{-1} (P–S–P bend), 272 cm^{-1} (P–S–P wag), 306 cm^{-1} (P–S–P wag), and 690/718 cm^{-1} (P═S stretch; double signal).

For years, it has been generally accepted that during thionation reactions, P_4S_{10} would dissociate into ionic P_2S_5 under reflux conditions in polar solvents.[18] The solubility experiment presented in this work demonstrates that this is not the case when P_4S_{10} is heated above reflux temperatures in ACN. Alternatively, P_4S_{10} conserves its structure under reflux conditions in ACN, as shown in this work *via in situ* Raman spectroscopy at elevated temperatures in a microwave reactor.

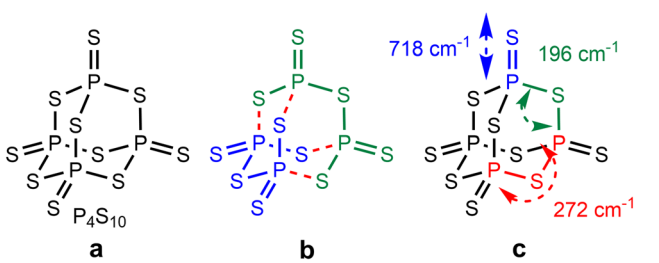

Fig. 2 (a) Native state of P_4S_{10}, (b) dimerized P_2S_5, and (c) the Raman signals associated with the structure of P_4S_{10}.

Furthermore, for clarity, P_2S_5 will be discussed as P_4S_{10} (with corrected molar stoichiometry) for the remainder of this manuscript.

To further investigate the Raman signals under the reaction conditions, the concentration standards of P_4S_{10} in ACN were analyzed. The objective of analyzing milled powders of P_4S_{10} was to establish a limit-of-detection (LOD) and a limit-of-quantification (LOQ) for the Raman spectrometer under reaction conditions, which is imperative for analytical experiments. For this experiment, the double signal at 718–690 cm^{-1} was selected for quantitative experiments because it exists in a region of spectral data that does not have any overlapping signals from ACN and is within close proximity to flat background noise that can be used for determining a signal-to-noise ratio (SNR).

The SNR for each concentration was determined using the conventional method of the mean signal intensity in the region (700–730 cm^{-1}) divided by the standard deviation of the intensity in the noise region (590–620 cm^{-1}). Subsequently, the plotted data of the SNR *vs.* the concentration of each standard in Fig. S2b allowed for the determination of the LOD and LOQ. Conventionally, the LOD and LOQ are equal to 3 and 10 SNR, respectively. Therefore, the signal at 718 cm^{-1} from *in situ* Raman measurements under the reaction conditions revealed a LOD and LOQ of 0.78 and 2.60 mM, respectively. The common functionality of a LOD and LOQ is primarily for analytical experiments; however this can also be used to determine when to stop taking measurements if analyzing spectra for kinetic changes in signals. If or when the signal of interest reaches the LOQ during kinetic experiments there is sufficient justification to exclude any following results due to the presence of measurement error.

With the determined LOD and LOQ, the experiments proceeded with the addition of Li_2S to the reaction system. The 3 LPS systems investigated were $1Li_2S$–$1P_4S_{10}$, $2Li_2S$–$1P_4S_{10}$, and $3Li_2S$–$1P_4S_{10}$, all under identical conditions and described in the Experimental section. During each reaction trial, there were noticeable changes in the signals associated with P_4S_{10}, which were not observed during solvation analysis. Fig. 3 shows the 3 respective LPS systems with the first and last spectra of the reaction for the P═S stretch signal at 716 cm^{-1} (a nominal shift from 718 cm^{-1} and assigned accordingly).

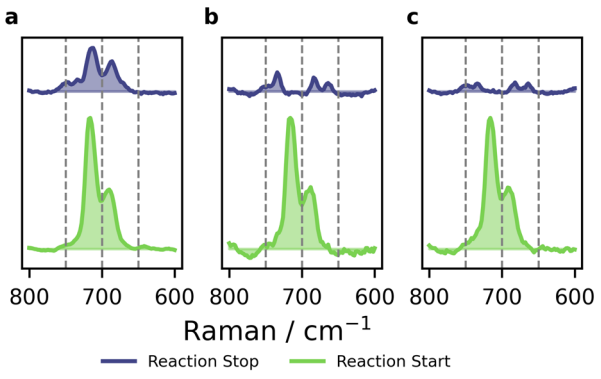

Fig. 3 (a) $1Li_2S$–$1P_4S_{10}$, (b) $2Li_2S$–$1P_4S_{10}$, and (c) $3Li_2S$–$1P_4S_{10}$ all recorded at 35 °C showing the Raman spectra between 600 and 800 cm^{-1} at the reaction start and reaction stop.

Like the other Raman signals attributed to P_4S10, the band at 716 cm^{-1}—associated with P═S stretching—gradually decreases in intensity across all reaction conditions. However, in the 2 : 1 and 3 : 1 Li_2S : P_4S_{10} systems, the signal either degrades to below the limit of detection or undergoes a pronounced shift to approximately 680 cm^{-1} by the end of the reaction. The 716 cm^{-1} feature is commonly attributed to P═S stretching vibrations and is particularly prominent due to the high symmetry and rigidity of the P_4S_{10} cage-like structure. As the structure becomes increasingly disrupted during the course of the reaction—either by ring opening or full conversion to thiophosphate intermediates—the intensity of this band diminishes correspondingly. Interestingly, this same spectral transformation was also observed, albeit unrecognized, in a separate study by Wang *et al.*[7] investigating LPS synthesis in acetonitrile. In that work, the authors proposed a mechanistic pathway wherein P_4S_{10} reacts with Li_2S to form $Li_2P_4S_{11}$ as an early intermediate in the solution-phase formation of $Li_7P_3S_{11}$, consistent with a glass-type thiophosphate condensation reaction.

$$Li_2S + P_4S_{10} \rightarrow Li_2P_4S_{11} \quad (1)$$

Like the experiments presented here, their reaction system $1Li_2S$–$1P_4S_{10}$ also preserved the signal at 716 cm^{-1}. Likewise, their additional reaction systems of 2 : 1 and 3 : 1 Li_2S : P_4S_{10} showed total signal degradation. However, since there is significant signal degradation in the 1 : 1 system the signal likely arises from the structural rigidity of P_4S_{10} as mentioned earlier.

By modeling the reaction mechanism as previously proposed for the $1Li_2S$–$1P_4S_{10}$ system in ACN, the structural integrity of P_4S_{10} can be analyzed. Scheme 1 presents the reaction mechanism described in eqn (1).

Following the reaction between Li_2S and P_4S_{10}, the resulting $Li_2P_4S_{11}$ species depicted in Scheme 1 retains considerable structural integrity due to its bicyclic configuration. The energy barrier required to distort or invert this structure is likely higher than the thermal energy available under the experimental conditions. Upon further reaction with additional Li_2S, the bicyclic compound may undergo a ring-

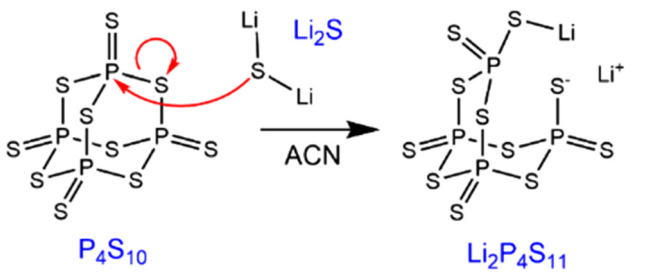

Scheme 1 The reaction mechanism for $1Li_2S$–$1P_4S_{10}$ in acetonitrile in a partially coordinated state with Li^+.

opening process with two plausible mechanistic pathways. If the P–S bond cleavage occurs at one of the terminal phosphorus atoms, the system is expected to relax into a monocyclic core with a thiophosphate side group. Alternatively, if bond cleavage takes place at a bridging phosphorus atom, the structure may expand into a single, larger ring. While this simplified model does not consider potential side reactions involving excess Li_2S or trace contaminants, such scenarios represent additional mechanistic complexity and are not addressed in this work. The key conclusion here is that the structural motifs responsible for the Raman band at 716 cm^{-1} are sufficiently disrupted under 2 : 1 and 3 : 1 $Li_2S : P_4S_{10}$ conditions, resulting in total signal loss, indicating complete degradation of the original framework.

There is also the possibility that the signal at 716 cm^{-1} shifts, as well as degrades, as previously mentioned. Fig. 3b and c both exhibit small double signals at 680 cm^{-1} with a similar shape to the double signal at 716 cm^{-1}. If there exist ionic compounds when Li_2S reacts with P_4S_{10} the π-bond of P═S can delocalize, stabilizing the negative charge on S^-. Subsequently, electron delocalization is a common culprit for signal shifts in Raman and IR spectroscopy.

By following the reaction mechanism in Scheme 1 and analyzing time-resolved spectra at controlled temperatures using a microwave reactor, kinetic information about the reaction systems can be obtained. Fig. 4 illustrates the time-resolved spectral analysis of a $1Li_2S$–$1P_4S_{10}$ reaction system in ACN.

The change in the signal observed at 716 cm^{-1} described in Fig. 4a allows for further examination of reaction dynamics, as illustrated in Fig. 4b.

To date, there are no reported reaction kinetics for the synthesis of LPS in liquid-phase processes. Presumably, this is due to the complicated reaction process, which involves reacting solid precursor chemicals in solvents, which then partially or fully dissociate. During the reaction these solvated or partially solvated intermediates precipitate in the presence of additional Li_2S, forming Li_3PS_4/solvent complexes. Subsequently, there are many factors that potentially influence the kinetics of these processes, including solvent type, temperature, particle size and morphology. However, if the overall process is divided into more controllable stages, then a clearer picture of the process and kinetics may be elucidated.

LPS systems in ACN have been reported to form soluble intermediates depending on the molar stoichiometry of the precursor reagents $Li_2S : P_4S_{10}$. Experiments performed at 1 : 1 and 2 : 1 molar ratios, respectively, have demonstrated high, if not complete, solubility in ACN.[6,7] Consequently, these 2 molar stoichiometries coincide with the reaction stoichiometries presented in this work, which bolster the claim that the change in the Raman signal observed at 716 cm^{-1} corresponds to the change in the molecular structure of P_4S_{10} as it reacts with Li_2S.

Accordingly, the time-resolved Raman spectra were integrated between 700 and 730 cm^{-1}, and evaluated for reaction kinetics.

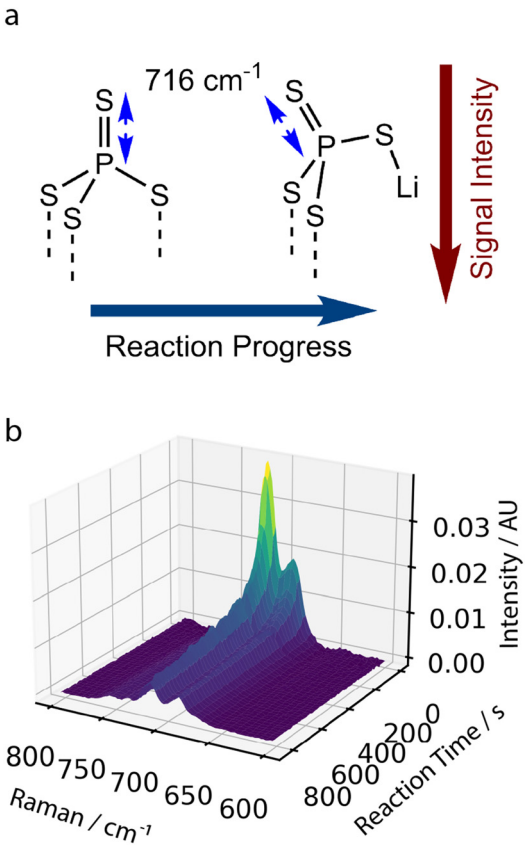

Fig. 4 (a) The change in signal intensity at 716 cm^{-1} as described in the reaction mechanism of Scheme 1, where the intensity decreases as the reaction progresses. (b) A 3D surface plot of the change in the signal at 716 cm^{-1}.

Early-stage reaction kinetics

The Finke–Watzky (FW) kinetic model was first introduced in 1997 as a mathematical framework to describe nanoparticle growth kinetics, particularly in systems exhibiting sigmoidal reaction profiles.[19] Originally developed to model particle aggregation, this approach has since been refined to provide physical meaning to its rate constants,[20] and has found broad applications in nanoparticle synthesis and protein aggregation studies.[21]

The FW model describes two elementary steps that together account for the observed sigmoidal behaviour: (1) a slow nucleation step A → B with rate constant k_1, and (2) an autocatalytic growth step A + B → 2B with rate constant k_2. In the context of nanoparticle growth, these steps represent the initial formation of critical nuclei followed by rapid, self-accelerating particle growth. The corresponding reaction curve typically displays a lag phase (slow nucleation), a transition or inflection point (onset of autocatalytic growth), a growth phase (rapid increase in product formation), and a plateau phase (reaction completion due to precursor depletion). This framework has proven particularly useful for understanding the interplay between nucleation kinetics, precursor consumption, and particle growth.

Notably, the FW model is mathematically flexible and may also describe particle degradation or dissolution, provided the same mechanistic conditions are met: a slow, spontaneous reaction followed by an autocatalytic process. In such cases, the sigmoidal curve is simply reversed in direction. The initial "lag phase" corresponds to a period of slow degradation, followed by a rapid decrease in concentration as autocatalytic mechanisms accelerate the process, culminating in a plateau once degradation reaches equilibrium.

This reversed application is particularly relevant to the solution-phase reaction between P_4S_{10} and Li_2S in acetonitrile (ACN). While P_4S_{10} is largely insoluble in ACN, it rapidly reacts with Li_2S to form soluble thiophosphate intermediates. These reactions likely proceed *via* particle surface interactions, where Li_2S progressively reduces the solid P_4S_{10} particles over time until equilibrium is reached. Mechanistic studies, such as that of Wang *et al.*, propose that the reaction initiates *via* opening of the cage-like P_4S_{10} structure.[7] This structural rearrangement decreases steric hindrance around phosphorus atoms, enhancing the accessibility of positively polarized P centers to nucleophilic attack by Li_2S, thereby accelerating the reaction through an autocatalytic pathway.

By analogy with the FW model, we may define A = P_4S_{10}, and B = $P_4S_{11}{}^{2-}$, where:

1. A → B represents the initial spontaneous breakdown of P_4S_{10} with the rate constant k_1 and
2. A + B → 2B captures the autocatalytic enhancement of this process with the rate constant k_2.

The differential rate law is given as:

$$-\frac{\mathrm{d}[\mathrm{A}]_t}{\mathrm{d}t} = \frac{\mathrm{d}[\mathrm{B}]_t}{\mathrm{d}t} = k_1[\mathrm{A}]_t + k_2[\mathrm{A}]_t[\mathrm{B}]_t \quad (1)$$

The corresponding integrated rate expressions are:

$$[\mathrm{A}]_t = [\mathrm{A}]_0 \frac{k_1 + k_2[\mathrm{A}]_0}{k_2[\mathrm{A}]_0 + k_1 \mathrm{e}^{(k_1+k_2[\mathrm{A}]_0)t}} \quad (2)$$

$$[\mathrm{B}]_t = [\mathrm{A}]_0 \left(1 - \frac{k_1 + k_2[\mathrm{A}]_0}{k_2[\mathrm{A}]_0 + k_1 \mathrm{e}^{(k_1+k_2[\mathrm{A}]_0)t}}\right) \quad (3)$$

Although direct observation of the intermediate species $Li_2P_4S_{11}$ by Raman spectroscopy is not feasible—due to a lack of unique diagnostic peaks—monitoring the decay of the P═S stretching mode at 716 cm^{-1} provides a reliable proxy. This band corresponds to the P_4S_{10} structure, and its diminishing intensity during the reaction indicates progressive consumption of the precursor. By tracking the integrated Raman intensity of this peak over time, the FW model can be fitted to extract meaningful kinetic parameters (Fig. 5a).

Additional temperature studies were performed and ln(k) was plotted in an Arrhenius relationship with the inverse of temperature (Fig. S2). The activation energy of each system was determined for the initial reaction step using the Arrhenius relationship between k and E_a(mw):

$$k = A\mathrm{e}^{-E_a(\mathrm{mw})/(RT)} \quad (4)$$

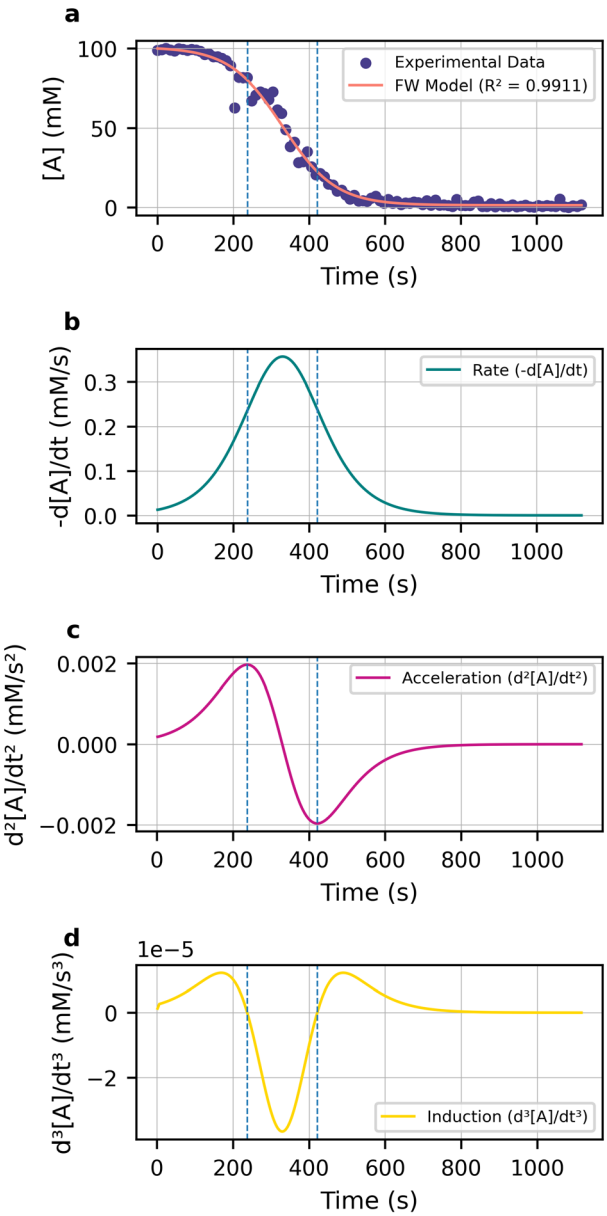

Fig. 5 (a) The decay of the 716 cm^{-1} Raman signal over time, fitted using the FW model. (b) The first derivative −d[A]/dt, which captures the time-dependent reaction rate. (c) The 2nd derivative (d^2[A]/dt^2) illustrating the acceleration points in the reaction. (d) The 3rd derivative (d^3[A]/dt^3) representing the induction (jerk) phase in the reaction. The fit yielded an R^2 = 0.9911, with rate constants k_1 = 3.99 × 10^{-4} s^{-1} and k_2 = 9.71 × 10^{-5} mM s^{-1} at 40 °C. The peak of the first derivative curve (Fig. 5b) corresponds to the maximum rate of degradation, confirming the sigmoidal behavior and autocatalytic character of the reaction.

where A is a pre-exponential factor determined from the fitted line, R is the universal gas constant and T is absolute temperature.

Additional thermodynamic parameters ($\Delta H^{\ddagger}$ and $\Delta S^{\ddagger}$) were extracted (Fig. S3) using the Eyring relationship:

$$k = \frac{k_B T}{h} \mathrm{e}^{-\frac{\Delta H^{\ddagger}}{RT}} \mathrm{e}^{\frac{\Delta S^{\ddagger}}{R}} \quad (5)$$

where k_B and h are the Boltzmann and Planck constants, respectively. The Arrhenius and Eyring analyses yield E_a(mw) = 39.59 kJ mol^{-1}, $\Delta H^{\ddagger}$ = 36.97 kJ mol^{-1}, and $\Delta S^{\ddagger}$ = −178.55 J mol^{-1} K^{-1}. These values indicate a modest activation barrier and an ordered transition state, consistent with rapid nucleation and growth under microwave-assisted conditions. The enthalpy of activation is slightly lower than E_a(mw), as expected, reflecting the true energetic requirement for forming the transition state complex. The strongly negative entropy of activation suggests that the transition state is more ordered than the reactants, likely arising from precursor alignment and restructuring at particle surfaces before bond reorganization occurs. Taken together, these parameters imply an energetically accessible but entropically disfavored process, a behavior typical of solid–solid or solid–liquid interfacial reactions where molecular mobility is constrained. This analysis confirms that the *in situ* Raman–kinetic framework provides robust parameter extraction and a reliable basis for mechanistic interpretation, while also highlighting that the addition of further Li_2S may modulate equilibria and kinetics, in agreement with Le Chatelier's principle.

Another important caveat of this experiment is that the reported activation energy corresponds to microwave-assisted conditions, E_a(mw), rather than the conventional activation energy. Microwave irradiation is known to reduce the apparent activation barrier of chemical reactions,[22] thereby accelerating reaction kinetics. It is therefore essential to clarify that the extracted kinetic and thermodynamic parameters reflect a reaction conducted under microwave assistance. Nevertheless, this analysis demonstrates that the Finke–Watzky (FW) model can be effectively extended beyond growth kinetics to capture particle degradation processes involving thiophosphate intermediates in polar aprotic solvents such as acetonitrile (ACN). In doing so, it provides both a physical and mathematical framework for describing the early-stage reaction kinetics of lithium thiophosphates (LPS).

Late-stage reaction kinetics

Raman spectroscopy has long been employed in the characterization of several types of sulfide solid electrolytes following synthesis, such as LPS and LPSC. A reported characteristic peak at approximately 420 cm^{-1} has long been attributed to PS_4^{3-}, a tetrahedral atomic structure found in most high-performance sulfide solid electrolytes like β-Li_3PS_4, $Li_7P_3S_{11}$, and Li_6PS_5Cl.

Although these electrolytes exhibit these characteristic signals which can confirm the microstructure of the synthesized SSEs, there lacks evidence of the progression of these signals during the synthesis process. To help better understand the formation of PS_4^{3-}, LPS and LPSC were monitored *in situ* at various reaction temperatures for 24 h (Fig. 6a and b).

Fig. 6a and b illustrate the integration of the normalized peak at 420 cm^{-1} with a 785 nm laser during the reactions of $3Li_2S$–$0.5P_4S_{10}$ and $5Li_2S$–$0.5P_4S_{10}$–2LiCl, respectively. The normalized intensity is achieved with respect to the acetonitrile solvent vibrational node at 920 cm^{-1} (Fig. S5 and S6), associated with C–C bonds in acetonitrile.[17] Additionally, acetonitrile exhibits a vibrational node centered at 382 cm^{-1} with an overlap upwards of 430–440 cm^{-1} (the same range as that of PS_4^{3-}). The non-zero values observed in Fig. 6a and b are attributed to this overlapping of signals; thus reliable observations are derived from the change in intensity from this baseline. This overlap was accounted for by applying a baseline correction to the kinetic model as illustrated by the dashed red line in Fig. 6a and b. The initial mixing of the particles in the solvent tends to contribute noise in the first few seconds and minutes of the reactions with higher concentrations of Li_2S, which can also contribute to the shift in intensity.

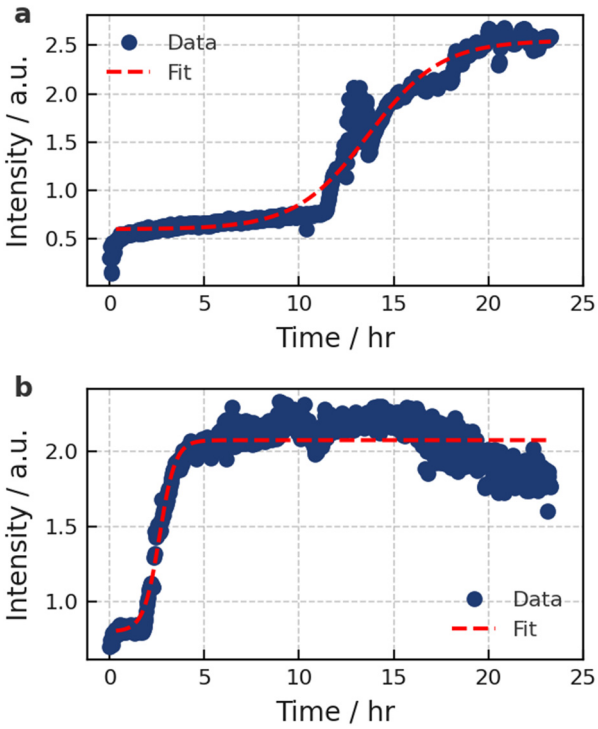

Fig. 6 (a) The reaction progress of $3Li_2S$–$0.5P_4S_{10}$ at 70 °C for 24 hours under microwave irradiation, and (b) the reaction progress of $5Li_2S$–$0.5P_4S_{10}$–2LiCl at 70 °C for 24 hours under microwave irradiation, both in acetonitrile.

A clear distinction in the late-stage reaction kinetics (monitored through the PS_4^{3-} signal) is that the sigmoidal reaction profile is inverted compared to that in the early stages. As expected, PS_4^{3-} does not appear during the initial phase but emerges later in the reaction. In Fig. 6a, its formation in LPS begins only after approximately 12 hours, followed by a very sharp acceleration. Similarly, in Fig. 6b, the onset of PS_4^{3-} formation in LPSC occurs almost instantaneously, which leads to a poor fit with the FW model.

Both LPS and LPSC exhibit the characteristic stages described by the Finke–Watzky (FW) kinetic framework: (i) an initial slow nucleation period, (ii) an acceleration phase, (iii) a growth phase, and (iv) final equilibration to a plateau. The flexible nature of the FW model also allows for a physical interpretation of these late-stage kinetic behaviors.

The PS_4^{3-} species has been widely reported only in the solid phase and has not yet been detected in the liquid phase in acetonitrile (ACN). Instead, under reaction conditions, PS_4^{3-} is known to form solid-phase complexes with lithium and solvent molecules.[23,24] Because the "B" species in the FW model was originally defined by Finke and Watzky as a growing or aggregated product, it is reasonable to assign "B" to the ACN/Li_3PS_4 complex in this system. Accordingly, "A" represents the chemical intermediate that precedes the formation of this complex.

Therefore, any kinetic or thermodynamic parameters derived from the integration of the 426 cm^{-1} Raman band correspond to the step associated with the generation of the ACN/Li_3PS_4 complex. Given that the literature still presents inconsistencies in the proposed mechanisms for lithium thiophosphate synthesis, the plateaus observed in Fig. 6a and b are better interpreted as qualitative indicators of reaction completion. Furthermore, because the acceleration phase occurs almost instantaneously, applying the FW model to describe PS_4^{3-} formation in either system introduces substantial fitting error.

Given the critical role of PS_4^{3-} in thiophosphate electrolytes, the equilibration of its Raman band at 420 cm^{-1} can be taken as an indication that the reaction has effectively terminated. Importantly, if the reaction is prolonged under aggressive conditions (*e.g.*, elevated temperature, microwave irradiation, or ultrasonication), PS_4^{3-} becomes increasingly susceptible to undesirable side reactions such as phosphorus reduction or sulfur oxidation. Indeed, Fig. 6b shows a decline in the PS_4^{3-} signal after ~15 hours, suggesting that such degradation pathways consume the species. $P_2S_6^{2-}$ (385 cm^{-1}) and $P_2S_6^{4-}$ (380 cm^{-1}),[25] both reported decomposition products of lithium thiophosphate systems, could be the culprit in signal deterioration at 426 cm^{-1}, but these species share overlapping signals with P_4S_{10} (392 cm^{-1}) and ACN (382 cm^{-1}), making it difficult to discriminate between the species during *in situ* experiments. However, the synthesized electrolytes can be further processed and analyzed *ex situ* which will remove the solvent signals after drying and elucidate other thiophosphate functional groups. As expected, decomposition products can be observed in the dried LPSC powders with Raman spectroscopy as shown in Fig. S7c at approximately 375 and 385 cm^{-1}, both of which likely correspond to $P_2S_6^{2-}$ (385 cm^{-1}) and $P_2S_6^{4-}$ (380 cm^{-1}). Albeit the obstacles, these observations underscore the utility of *in situ* monitoring to determine optimal reaction times, enabling more efficient syntheses while minimizing the risk of unwanted reactions.

Conclusion

In situ Raman spectroscopy under microwave control enables direct, real-time tracking of the Li_2S + P_4S_{10} thiophosphate reaction in acetonitrile, providing a powerful means of correlating molecular-scale vibrational signatures with kinetic models. The Finke–Watzky framework successfully captures the early-stage evolution of the P═S (716 cm^{-1}) band, offering clear evidence of nucleation and growth processes occurring during precursor conversion. Temperature-dependent analyses further refine this understanding, yielding Arrhenius and Eyring parameters of E_a(mw) = 39.59 kJ mol^{-1}, $\Delta H^{\ddagger}$ = 36.97 kJ mol^{-1}, and $\Delta S^{\ddagger}$ = −178.55 J mol^{-1} K^{-1}, which together indicate an energetically accessible pathway accompanied by a highly ordered transition state.

Beyond parameter extraction, the workflow integrates several practical features that enhance its utility: the determination of analytical benchmarks such as the LOD/LOQ, quantitative assessment of rate constants and their derivatives, and systematic comparison across multiple stoichiometries (1 : 1, 2 : 1, and 3 : 1) under identical conditions. This multifaceted approach not only validates the robustness of the methodology but also highlights its versatility in dissecting both chemical and physical aspects of sulfide electrolyte formation.

Importantly, the insights obtained here extend well beyond the specific Li_2S–P_4S_{10} system. The combination of *in situ* vibrational spectroscopy, microwave-assisted synthesis, and kinetic modelling establishes a generalizable platform for real-time process elucidation and optimization in liquid-phase routes to sulfide solid electrolytes. Such a framework can be readily adapted to explore alternative solvents, precursors, or dopants, as well as applied to emerging families of halide or oxide solid electrolytes. Furthermore, coupling Raman with complementary *in situ* probes (XRD, NMR, or IR) holds significant potential for building a comprehensive picture of intermediate speciation and structural evolution. Ultimately, this integrated strategy advances both the fundamental mechanistic understanding and the practical design principles required for scalable, reproducible, and high-performance solid electrolyte synthesis.

Author contributions

The manuscript was written by Z. Warren. The concept was developed by Z. Warren and N. C. Rosero-Navarro. Experiments were performed by Z. Warren, T. Poupeau, and B. Batu. Supervision and funding acquisition were carried out by N. C. Rosero-Navarro. All authors have given approval to the final version of the manuscript.

Conflicts of interest

There are no conflicts to declare.

Abbreviations

ASSLiB(s)	All-solid-state lithium-ion battery(ies)
LIB(s)	Lithium-ion battery(ies)
SSE(s)	Solid-state electrolyte(s)
LPS	Lithium thiophosphate (family of sulfide electrolytes; *e.g.*, Li_3PS_4/$Li_7P_3S_{11}$)

LPSX	Halogen-substituted lithium thiophosphates (X = Cl, Br, I)
LPSC	Lithium thiophosphate chloride (commonly Li_6PS_5Cl, argyrodite)
ACN	Acetonitrile
pSSE(s)	Pre-solid-state electrolyte(s) (pre-sulfide mixtures)
FW (model)	Finke–Watzky kinetic model
LOD	Limit of detection
LOQ	Limit of quantification
SNR	Signal-to-noise ratio
XRD	X-ray diffraction
IR	Infrared (spectroscopy)
NMR	Nuclear magnetic resonance
SEM	Standard error of the mean
E_a(mw)	Microwave-assisted activation energy
$\Delta H^{\ddagger}$	Enthalpy of activation
$\Delta S^{\ddagger}$	Entropy of activation

Data availability

The datasets generated and analyzed during the current study are not yet available in a public repository.

Upon publication of this article, all raw and processed data will be deposited in the institutional repository of the Institute of Ceramic and Glass of the CSIC and will be accessible at **https://digital.csic.es/**.

Until that time, the data are available from the corresponding author upon reasonable request.

Supplementary information (SI): calibration benchmarks for the Raman spectrometer, Arrhenius and Eyring analyses, statistical parameters, and Raman spectra corresponding to Fig. 6. See DOI: **https://doi.org/10.1039/d5qi01971k**.

Acknowledgements

This research work is a part of the PIE project "Innovative and Designed (Electro)-Chemistry, All-in-One for Lithium Sulfide Solid Electrolytes" (IDEAL-Li), reference 20226AT009, supported by The Spanish National Research Council (CSIC). This work was supported by the ELISA project (ref. CNS2023-145494), funded by MCIN/AEI/10.13039/501100011033 and by the European Union "NextGenerationEU"/PRTR. We also acknowledge the Erasmus Internship support for Thomas Poupeau and Beyza Batu.

References

1 Y.-Y. Sun, F. Li and P.-Y. Hou, Research progress on the interfaces of solid-state lithium metal batteries, *J. Mater. Chem. A*, 2021, **9**(15), 9481–9505, DOI: **10.1039/d1ta00467k**.

2 M. Yao, J. Shi, A. Luo, Z. Zhang, G. Zhu, H. Xu, J. Xu, L. Jiang and K. Jiang, Advances in sulfide solid–state electrolytes for lithium batteries, *Energy Storage Mater.*, 2025, **75**, 104018, DOI: **10.1016/j.ensm.2025.104018**.

3 M. A. Kraft, S. Ohno, T. Zinkevich, R. Koerver, S. P. Culver, T. Fuchs, A. Senyshyn, S. Indris, B. J. Morgan and W. G. Zeier, Inducing High Ionic Conductivity in the Lithium Superionic Argyrodites $Li_{6+x}P_{1-x}Ge_xS_5I$ for All-Solid-State Batteries, *J. Am. Chem. Soc.*, 2018, **140**(47), 16330–16339, DOI: **10.1021/jacs.8b10282**.

4 R. Rajagopal, Y. Subramanian, Y. J. Jung, S. Kang and K.-S. Ryu, Rapid Synthesis of Highly Conductive Li_6PS_5Cl Argyrodite-Type Solid Electrolytes Using Pyridine Solvent, *ACS Appl. Energy Mater.*, 2022, **5**(8), 9266–9272, DOI: **10.1021/acsaem.2c01157**.

5 J. Zhou, Y. Chen, Z. Yu, M. Bowden, Q. R. S. Miller, P. Chen, H. T. Schaef, K. T. Mueller, D. Lu, J. Xiao, *et al.*, Wet-chemical synthesis of $Li_7P_3S_{11}$ with tailored particle size for solid state electrolytes, *Chem. Eng. J.*, 2022, **429**, 132334, DOI: **10.1016/j.cej.2021.132334**.

6 M. Calpa, N. C. Rosero-Navarro, A. Miura, K. Terai, F. Utsuno and K. Tadanaga, Formation Mechanism of Thiophosphate Anions in the Liquid-Phase Synthesis of Sulfide Solid Electrolytes Using Polar Aprotic Solvents, *Chem. Mater.*, 2020, **32**(22), 9627–9632, DOI: **10.1021/acs.chemmater.0c03198**.

7 Z. Wang, Y. Jiang, J. Wu, Y. Jiang, S. Huang, B. Zhao, Z. Chen and J. Zhang, Reaction mechanism of Li_2S-P_2S_5 system in acetonitrile based on wet chemical synthesis of $Li_7P_3S_{11}$ solid electrolyte, *Chem. Eng. J.*, 2020, **393**, 124706, DOI: **10.1016/j.cej.2020.124706**.

8 H. Gamo, J. Nishida, A. Nagai, K. Hikima and A. Matsuda, Solution Processing via Dynamic Sulfide Radical Anions for Sulfide Solid Electrolytes, *Adv. Energy Sustainability Res.*, 2022, **3**(7), 2200019, DOI: **10.1002/aesr.202200019**.

9 Z. Warren and N. C. Rosero-Navarro, Solution-Based Suspension Synthesis of Li_2S–P_2S_5 Glass-Ceramic Systems as Solid-State Electrolytes: A Brief Review of Current Research, *ACS Omega*, 2024, **9**(29), 31228–31236, DOI: **10.1021/acsomega.4c03784**.

10 C. Dietrich, D. A. Weber, S. Culver, A. Senyshyn, S. J. Sedlmaier, S. Indris, J. Janek and W. G. Zeier, Synthesis, Structural Characterization, and, Lithium Ion Conductivity of the Lithium Thiophosphate $Li_2P_2S_6$, *Inorg. Chem.*, 2017, **56**(11), 6681–6687, DOI: **10.1021/acs.inorgchem.7b00751**.

11 M. Ghidiu, R. Schlem and W. G. Zeier, Pyridine Complexes as Tailored Precursors for Rapid Synthesis of Thiophosphate Superionic Conductors, *Batteries Supercaps*, 2021, **4**(4), 607–611, DOI: **10.1002/batt.202000317**.

12 B. Fan, Q. Zhang, Z. Luo, X. Zhang, H. Ma, P. Fan and B. Xue, Influence of precipitate/supernatant ratio during liquid-phase synthesis of solid electrolyte $Li_7P_3S_{11}$, *Solid State Ionics*, 2019, **343**, 115073, DOI: **10.1016/j.ssi.2019.115073**.

13 M. Calpa, N. C. Rosero-Navarro, A. Miura and K. Tadanaga, Instantaneous preparation of high lithium-ion conducting sulfide solid electrolyte $Li_7P_3S_{11}$ by a liquid phase process,

RSC Adv., 2017, **7**(73), 46499–46504, DOI: **10.1039/c7ra09081a**.

14 M. B. Gawande, S. N. Shelke, R. Zboril and R. S. Varma, Microwave-assisted chemistry: synthetic applications for rapid assembly of nanomaterials and organics, *Acc. Chem. Res.*, 2014, **47**(4), 1338–1348, DOI: **10.1021/ar400309b**.

15 A. Miura, N. C. Rosero-Navarro, A. Sakuda, K. Tadanaga, N. H. H. Phuc, A. Matsuda, N. Machida, A. Hayashi and M. Tatsumisago, Liquid-phase syntheses of sulfide electrolytes for all-solid-state lithium battery, *Nat. Rev. Chem.*, 2019, **3**(3), 189–198, DOI: **10.1038/s41570-019-0078-2**.

16 J. O. Jensen and D. Z. Theoretical, studies of the infrared and Raman spectra of P_4S_{10}, *J. Mol. Struct.: THEOCHEM*, 1999, **487**, 267–274, DOI: **10.1016/S0166-1280(99)00068-8**.

17 S. Zhang, H. Jia, M. Song, H. Shen, L. Dongfei and L. Haibo, Raman spectroscopy study of acetonitrile at low temperature, *Spectrochim. Acta, Part A*, 2021, **246**, 119065, DOI: **10.1016/j.saa.2020.119065**.

18 T. Ozturk, E. Ertas and O. Mert, A Berzelius Reagent, Phosphorus Decasulfide (P_4S_{10}), in Organic Synthesis, *Chem. Rev.*, 2010, (110), 3419–3478, DOI: **10.1021/cr900243d**.

19 M. Watzky and R. Finke, Transition Metal Nanocluster Formation Kinetic and Mechanistic Studies. A New Mechanism When Hydrogen Is the Reductant Slow, Continuous Nucleation and Fast Autocatalytic Surface Growth, *J. Am. Chem. Soc.*, 1997, **119**, 10382–10400.

20 L. Bentea, M. A. Watzky and R. G. Finke, Sigmoidal Nucleation and Growth Curves Across Nature Fit by the Finke–Watzky Model of Slow Continuous Nucleation and Autocatalytic Growth: Explicit Formulas for the Lag and Growth Times Plus Other Key Insights, *J. Phys. Chem. C*, 2017, **121**(9), 5302–5312, DOI: **10.1021/acs.jpcc.6b12021**.

21 S. Özkar and R. G. Finke, Silver Nanoparticles Synthesized by Microwave Heating: A Kinetic and Mechanistic Re-Analysis and Re-Interpretation, *J. Phys. Chem. C*, 2017, **121**(49), 27643–27654, DOI: **10.1021/acs.jpcc.7b06323**.

22 J. Zhou, W. Xu, Z. You, Z. Wang, Y. Luo, L. Gao, C. Yin, R. Peng and L. Lan, A new type of power energy for accelerating chemical reactions: the nature of a microwave-driving force for accelerating chemical reactions, *Sci. Rep.*, 2016, **6**, 25149, DOI: **10.1038/srep25149**.

23 N. H. H. Phuc, K. Morikawa, T. Mitsuhiro, H. Muto and A. Matsuda, Synthesis of plate-like Li_3PS_4 solid electrolyte via liquid-phase shaking for all-solid-state lithium batteries, *Ionics*, 2017, **23**(8), 2061–2067, DOI: **10.1007/s11581-017-2035-8**.

24 M. Calpa, H. Nakajima, S. Mori, Y. Goto, Y. Mizuguchi, C. Moriyoshi, Y. Kuroiwa, N. C. Rosero-Navarro, A. Miura and K. Tadanaga, Formation Mechanism of beta-Li_3PS_4 through Decomposition of Complexes, *Inorg. Chem.*, 2021, **60**(10), 6964–6970, DOI: **10.1021/acs.inorgchem.1c00294**.

25 C. Dietrich, M. Sadowski, S. Sicolo, D. A. Weber, S. J. Sedlmaier, K. S. Weldert, S. Indris, K. Albe, J. Janek and W. G. Zeier, Local Structural Investigations, Defect Formation, and Ionic Conductivity of the Lithium Ionic Conductor $Li_4P_2S_6$, *Chem. Mater.*, 2016, **28**(23), 8764–8773, DOI: **10.1021/acs.chemmater.6b04175**.

